

Matrix-LSTM: a Differentiable Recurrent Surface for Asynchronous Event-Based Data

Marco Cannici Marco Ciccone Andrea Romanoni Matteo Matteucci
Politecnico di Milano, Italy
{marco.cannici, marco.ciccone, andrea.romanoni, matteo.matteucci}@polimi.it

Abstract

Dynamic Vision Sensors (DVSs) asynchronously stream events in correspondence of pixels subject to brightness changes. Differently from classic vision devices, they produce a sparse representation of the scene. Therefore, to apply standard computer vision algorithms, events need to be integrated into a frame or event-surface. This is usually attained through hand-crafted grids that reconstruct the frame using ad-hoc heuristics. In this paper, we propose Matrix-LSTM, a grid of Long Short-Term Memory (LSTM) cells to learn end-to-end a task-dependent event-surfaces. Compared to existing reconstruction approaches, our learned event-surface shows good flexibility and expressiveness improving the baselines on optical flow estimation on the MVSEC benchmark and the state-of-the-art of event-based object classification on the N-Cars dataset.

1. Introduction

Event-based cameras, such as dynamic vision sensors (DVSs) [23, 39, 2, 33], are bio-inspired devices that attempt to emulate the efficient data-driven communication mechanisms of the brain. Unlike conventional frame-based active pixel sensors (APS), which synchronously capture the scene at a predefined and constant frame-rate, these devices are composed of independent pixels that output sequences of asynchronous events, efficiently encoding pixel-level brightness changes caused by objects moving inside the scene. This results in a sensor having a very high dynamic range (> 120 dB) and high temporal resolution (in the order of microseconds), matched with low power consumption and minimal delay. All these characteristics are key features in challenging scenarios involving fast movements (e.g., drones or moving cars), and abrupt brightness changes (e.g., when exiting a dark tunnel in a car).

However, novel methods and hardware architectures need to be specifically designed to exploit these advantages and leverage the full potential of event cameras in complex tasks. Event-cameras only provide a timed sequence of changes that is not directly compatible with computer vision

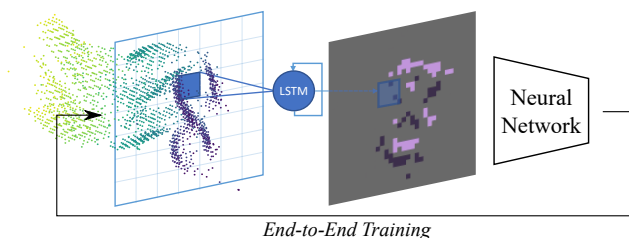


Figure 1. The Matrix-LSTM end-to-end differentiable surface applied on an N-MNIST [31] sample. Figure adapted from [30].

systems which indeed typically work on frames. In particular, since every single event is asynchronous, and it only carries a binary information (the occurrence of a change in a specific position and time instant), mechanisms able to effectively encode the precise timing information of events are key components of effective event-based vision systems, especially in data-driven pipelines.

Driven by the great success of frame-based deep learning architectures, that learn representations directly from standard APS signals, research in event-based processing is now focusing on how to effectively aggregate event information in grid-based representations which can be directly used, for instance, by convolutional deep learning models. Nevertheless, finding the best mechanism to extract information from event streams is not trivial, being representations usually task-specific. Multiple solutions have indeed emerged during the past few years, mostly employing hand-crafted mechanisms to accumulate events. Examples of such representations are mechanisms relying on exponential [8, 20, 40] and linear [8, 5] decays, “event-surfaces” storing the timestamp of the last received event in each pixel and extensions of such mechanism making use of memory cells [40] and voxel-grids [34, 48].

Only very recently deep learning techniques have been applied to learn such surfaces in a data-driven manner [13]. In this paper, we focus on this recent trend in event-based processing, and propose to apply a Long Short-Term Memory (LSTM) network [16] as a convolutional filter over the 2D stream of events to accumulate pixel information through time and extract pixel values for building 2D event

representations. The reconstruction mechanism is end-to-end differentiable, meaning that it can be used as input representation of any state-of-the-art frame-based architecture and jointly trained to learn event-surfaces specifically tailored for the task at hand.

Substituting hand-crafted event-surfaces with our trainable layer in state-of-the-art architectures improves their performance substantially without requiring particular effort in hyper-parameter tuning. The layer is a powerful drop-in replacement for hand-crafted event-surfaces, enabling researches to exploit event information effectively and improve the performance of existing architectures with minor modifications. The contributions of the paper are summarized as follows:

- We propose Matrix-LSTM, a task-independent mechanism to extract grid-like event representations from asynchronous streams of events. The framework is end-to-end differentiable, it can be used as input of any existing frame-based state-of-the-art architecture and jointly trained to extract the best representation from the events.
- Replacing input representations with a Matrix-LSTM layer in existing architectures, we show that it improves the state-of-the-art on event-based object classification on N-CARS [40] by 3.3% and performs better than hand-crafted features on N-Caltech101 [31]. Finally, it improves optical flow estimation on the MVSEC benchmark [49] up to 30.76% over hand-crafted features [49] and up to 23.07% over end-to-end differentiable ones [13].
- We developed custom CUDA kernels to efficiently aggregate events by position and perform a convolution-like operation on the stream of events using an LSTM as a convolutional filter. We finally implemented the Matrix-LSTM layer both in PyTorch [41] and TensorFlow [1] to enable easier integration of the proposed learnable surface in existing architectures¹.

2. Related Work

One of the key features underlying modern computer vision algorithms is their ability to aggregate elementary visual information to build complex visual features. To this end, convolutional neural networks (CNNs) are by far the most widespread method in frame-based architectures for image classification [15, 19, 42], object detection [14, 24, 35], semantic segmentation [7, 25, 46], and many others. Their great success resides on their end-to-end differentiable structure that allows these architectures to learn powerful visual representations for the task to be solved. Despite their advantages in terms of time resolution and dynamic range, the potentialities of event-based

cameras remain unlocked, mainly due to the difficulty of building good representations from sparser, asynchronous and much more rough source of information compared to frame-based data.

In this section we give a brief overview of related work on representations for event-based data, highlighting the differences and similarities with our work. We refer the reader to [11] for a thorough overview.

Spike-based representations. Initially, neural systems designed to perform spike-based computation, such as Spiking Neural Networks (SNNs) [26], have been applied to event-based processing in several tasks, e.g., edge detection [44, 28], object classification [21, 10] and hand-gestures recognition [4]. However, their non-differentiability and the lack of a well established supervised training procedure have limited the spreading of SNNs based architectures. Recent works [36] tried to overcome these limitations by first training a frame-based conventional neural network, and then convert its weights into SNNs parameters, managing to deal with complex structures such as GoogLeNet Inception-V3 [42]. Inspired by the event integration mechanism in SNNs, simple but effective, non-parametric leaky integration procedures have been proposed in recent work [5, 6, 8], where the reconstructed frame is increased of a fixed quantity whenever an event occurs in the position corresponding to the event address and linearly decayed otherwise.

Hand-crafted representations. Recently, the concept of “*time-surface*” was also introduced [20, 27], in which 2D surfaces are obtained by keeping track of the timestamp of the last event occurring in each location and by associating each event with temporal features computed applying exponential kernels on the event-surface. An extension of these methods, called HATS [40], makes use of memory cells retaining temporal information from past events. Instead of computing the surface using just the timestamp of the last event, too sensitive to noise, HATS uses a history of events in a temporal window of fixed length. Histograms of these activations are then computed to describe visual features and finally, a SVM classifier is used for prediction.

The use of an internal memory to compute the event-surface closely relates HATS with the solution presented in this paper. Crucially, the accumulation procedure employed in HATS is hand-crafted, while our work is end-to-end trainable thanks to a grid of LSTM cells [16] that learn the accumulation step. This allows the memory to potentially handle an infinite number of events, but more importantly to learn a better accumulation strategy directly from data.

In [48], the authors propose the EV-FlowNet network for optical flow estimation together with a new time-surface variant. Events of different polarities are kept separate to build a four-channel grid containing the number of oc-

¹Code of both implementations will be released after paper acceptance.

curred events in each location besides temporal information. A similar event representation has also been used in [45] to predict depth, ego-motion and optical flow from events. To improve the temporal resolution of such representations, [50] suggests to discretize the time dimension into consecutive temporal bins and accumulate events into a voxel-grid through a linearly weighted accumulation similar to bilinear interpolation. A similar time discretization has also been used in Events-to-Video [34], where the event representation is used within a recurrent-convolutional architecture to produce realistic video reconstructions of event sequences. Despite being slower than other methods, the quality of reconstructed frames closely resembles actual gray-scale frames, allowing the method to take full advantage from transferring feature representations trained on natural images.

End-to-end representations. Most closely related to the current work, [13] learns a dense representation end-to-end directly from raw events. A multi-layer perceptron (MLP) is used to implement a trilinear filter that produces a voxel-grid of temporal features. The event time information of each event is encoded using the MLP network and the value obtained from events occurring in the same spatial location are summed up together to build the final feature. A look-up table is then used, after training, to speed-up the integration procedure. Events are processed independently as elements of a set, disregarding their sequentiality and preventing the network to modulate the information conditioned on previous events. Our method, instead, by leveraging the memory mechanism of LSTM cells, can integrate information conditioned on the current state and can decide how much each event is relevant to perform the task, and how much information to retain from past events. Finally, a recent trend in event-based processing is studying mechanisms that do not require to construct intermediate explicit dense representations to perform the task at hand [3, 38, 43]. Among these, [30] uses a variant of the LSTM network, called PhasedLSTM, to learn the precise timings of events. While it integrates the events sequentially as in our work, PhasedLSTM employs a single cell on the entire stream of events and can be used only on very simple tasks [6]. The model, indeed, does not maintain the input spatial structure and condenses the 2D stream of events into a single feature vector, preventing the network to be used as input to standard CNNs. In contrast, in this paper we use the LSTM as a convolutional filter, thus, we obtain a translation-invariant module that integrates local temporal features independently while retaining spatial structures.

3. Method

Event-based cameras are vision sensors composed of pixels able to work independently. Each pixel has its own exposure time and it is free to fire independently by pro-

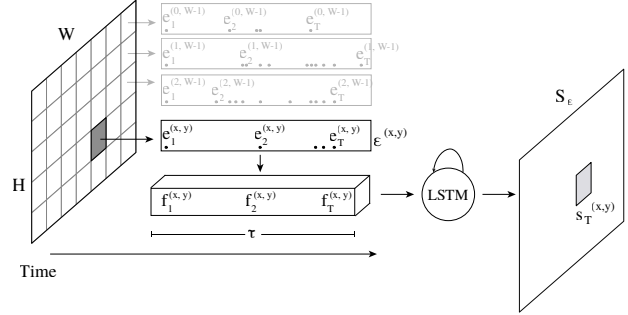


Figure 2. Overview of the proposed Matrix-LSTM module. Events in each pixel are first associated to a set of features $f_i^{(x,y)}$, one for each events. The sequence of features is processed by the LSTM and the output corresponding to the last value, $s_T^{(x,y)}$, is finally used to construct S_E .

ducing an event as soon as it detects a significant change in brightness. Unlike conventional devices, no rolling shutter is used, instead, an asynchronous stream of events is generated describing what has changed in the scene. Each event e_i is a tuple $e_i = (x_i, y_i, t_i, p_i)$ specifying the time t_i , the location $(x, y)_i$ (within a $H \times W$ space) and the polarity $p_i \in \{-1, 1\}$ of the change (brightness increase or decrease). Therefore, given a time interval τ (i.e., the sample length), the set of events produced by the camera can be described as a sequence $\mathcal{E} = \{(x_i, y_i, t_i, p_i) \mid t_i \in \tau\}$, ordered by the event timestamp. In principle, multiple events could be generated at the same timestamp. However, the grid representation of the events at a fixed timestamp t is likely to be very sparse, hence, an integrating procedure is necessary to reconstruct a dense representation S_E before being processed by conventional frame-based algorithms.

Note that, in this work, we do not aim to reconstruct a frame that resembles the actual scene, such as a grey-scale or RGB image [34, 37], but instead to extract task-aware features regardless of their appearance. In the following, “surface”, “reconstruction” and “representation” are used with this meaning.

3.1. Matrix-LSTM

Analogously to [13], our goal is to learn end-to-end a fully parametric mapping $\mathcal{M} : \mathcal{E} \rightarrow S_E \in \mathbb{R}^{H \times W \times C}$, between the event sequence and the corresponding dense representation, providing the best features for the task to optimize. In this work, we propose to implement \mathcal{M} as a $H \times W$ matrix of LSTM cells [16] (see Figure 2).

Let’s define the ordered sequence of events $\mathcal{E}^{(x,y)}$ produced by the pixel (x, y) during interval τ as $\mathcal{E}^{(x,y)} = \{(x_i, y_i, t_i, p_i) \mid t_i \in \tau, x_i = x, y_i = y\} \subset \mathcal{E}$, and its length as $T^{(x,y)} = |\mathcal{E}^{(x,y)}|$, which may potentially be different for each location (x, y) . A set of features $(x, y) f_i^{(x,y)} \in \mathbb{R}^F$ is first computed for each event occurring at location (x, y) , typically the polarity and one or multiple temporal features (see Section 4). At each location (x, y) , an $LSTM^{(x,y)}$ cell

then processes these input features asynchronously, keeping track of the current integration state and condensing all the events dynamics into a single output vector $s^{(x,y)} \in \mathbb{R}^C$.

In particular, at each time t , the $LSTM^{(x,y)}$ cell produces an intermediate representation $s_t^{(x,y)}$. Once all the events are processed, the last output of the LSTM cell compresses the dynamics of the entire sequence $\mathcal{E}^{(x,y)}$ into a fixed-length vector $s_T^{(x,y)}$ that can be used as pixel feature (here we dropped the superscript $^{(x,y)}$ from T for readability). The final surface $\mathcal{S}_{\mathcal{E}}$ is finally built by collecting all the LSTMs final outputs $s_T^{(x,y)}$ into a dense tensor of shape $H \times W \times C$. A fixed all-zeros output $s_T^{(x,y)}$ is used where the set of events $\mathcal{E}^{(x,y)}$ is empty.

Temporal bins. Taking inspiration from previous methods [13, 34, 50] that discretize the time dimension into temporal bins, we also propose a variant of the Matrix-LSTM module that operates on successive temporal windows to produce the final representation.

Given a fixed number of bins B , the original event sequence is split into B consecutive windows $\mathcal{E}_{\tau_1}, \mathcal{E}_{\tau_2}, \dots, \mathcal{E}_{\tau_B}$. Each sequence is processed independently, i.e., the output of each LSTM at the end of each interval is used to construct a representation $\mathcal{S}_{\mathcal{E}_b}$ and their state is re-initialized before the next sub-sequence starts. This gives rise of B different reconstructions $\mathcal{S}_{\mathcal{E}_b}$ that are concatenated to form the final reconstruction $\mathcal{S}_{\mathcal{E}} \in \mathbb{R}^{H \times W \times B \times C}$. In this formulation, the LSTM input features $f_i^{(x,y)}$ usually contain both global temporal features (i.e., w.r.t. the original uncut sequence) and relative features (i.e., the event position in the sub-sequence). Although LSTMs should be able to retain memory over very long periods, we found that discretizing time into intervals helps the Matrix-LSTM layer in maintaining event information, especially in tasks requiring rich and precise time information such as optical flow estimation (see Section 4.2). A self-attention module [17] is then optionally applied on the reconstructed surface to correlate intervals (see Section 4.1.1).

Parameters sharing. Inspired by the convolution operation defined on images, we designed the Matrix-LSTM layer to enjoy translation invariance by performing a local mapping of events into features. By sharing the parameters across the LSTM cells, we can consider Matrix-LSTM as a convolution operator over the 2D-grid streams of events applied with a 1×1 receptive field. Please, refer to the supplementary material for an extension of Matrix-LSTM on larger receptive fields. Events in each location are processed sequentially using the LSTM memory to accumulate values and perform conditioned integration. Taking advantage of the LSTM gating mechanism, the network can indeed learn the best integration strategy given the current state, i.e., deciding each time how to encode the current event based on all the previous history (e.g., using the timing information

to dynamically adapt to different event rates). Sharing the LSTM parameters, not only drastically reduces the number of parameters in the network, but it also allows us to transfer a transformation learned on a certain camera to any higher or lower resolution device by simply convolving the cell into a different spatial structure as in fully-convolutional networks [25].

We highlight the fact that such an interpretation of the Matrix-LSTM functioning also fits the general framework proposed in [13], in which popular event densification mechanisms are rephrased as kernel convolutions performed on an *event field*, i.e., a discretized four-dimensional manifold spanning the x and y spatial coordinates, and the time and polarity dimensions.

3.2. Implementation

The convolution-like operation described in the previous section can be implemented efficiently by means of two carefully designed event grouping operations. Rather than replicating the LSTM unit multiple times on each spatial location, a single recurrent unit is indeed applied over different $\mathcal{E}^{(x,y)}$ sequences in parallel. For each location, the LSTM cell has to process an ordered sequence of events, from the one having the smallest t_i to the last in the sequence. This requires a split operation that maintains the events' relative ordering within the pixels. We highlight that these operations are not specific to Matrix-LSTM, since grouping events by pixel index is a common operation in event-based processing, and could indeed benefit other event-based implementations making use of GPUs.

GroupByPixel. This operation translates from event-sequences to pixel-sequences. Let X be a tensor of shape $N \times T_{max} \times F$, representing the features $f_{n,i}^{(x,y)}$ of a batch of N samples, where T_{max} is the length of the longest sequence in the batch. We define the *groupByPixel* mapping on X as an order-aware reshape operation that rearranges the events into a tensor of pixel-sequences of shape $N * H * W \times T_{max}^{(x,y)} \times F$, where H, W are the spatial dimensions of the frame grid, and $T_{max}^{(x,y)}$ is the length of the longest pixel sequence $\mathcal{E}_n^{(x,y)}$. Pixel-sequences shorter than $T_{max}^{(x,y)}$ are padded with zero events to be processed in parallel. The operation extracts only pixel-sequences having at least one event, so the first dimension is usually smaller than $N * H * W$ (which is an upper bound).

The tensor thus obtained is then processed by the LSTM cell that treats samples in the first dimension independently, effectively implementing parameter sharing and applying the transformation in parallel over all the pixels. The LSTM output tensor, which has the same shape of the input one, is then sampled by taking the output corresponding to the last event in each pixel-sequence $\mathcal{E}_n^{(x,y)}$, ignoring values computed on padded values, and the obtained values are then

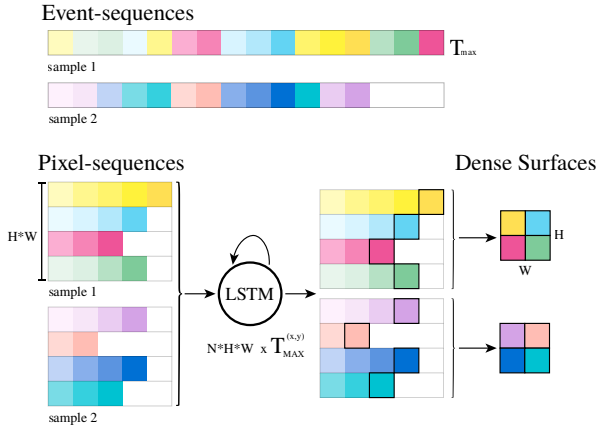


Figure 3. An example of the *groupByPixel* operation on a batch of $N = 2$ samples and a 2×2 pixel resolution. Different colors refer to different pixel locations while intensity indicates time. For clarity, the features dimension is not shown in the figure.

used to populate the dense representation. To improve efficiency, for each pixel-sequence $\mathcal{E}_n^{(x,y)}$, *groupByPixel* keeps also track of the original spatial position (x, y) , the index of the sample inside the batch and the length of the pixel-sequence $T_n^{(x,y)}$, namely the index of the last event before padding. Given this set of indexes, the densification step can be performed as a simple slicing operation. See Figure 3 for visual clues. *groupByPixel* is implemented as a custom CUDA kernel that processes each sample in parallel and places each event feature in the output tensor maintaining the original temporal order.

GroupByTime. The Matrix-LSTM variant that operates on temporal bins performs a similar pre-processing step. Each sample in the batch is divided into a fixed set of intervals. The *groupByTime* cuda kernel pre-processes the input events generating a $N * B \times T_{max}^b \times F$ tensor where bins are grouped in the first dimension and taking care of properly padding intervals (T_{max}^b is the length of the longest bin in the batch). The Matrix-LSTM mechanism is then applied as usual and the resulting $N * B \times H \times W \times C$ tensor is finally reshaped into a $N \times H \times W \times B * C$ event-surface.

4. Evaluation

Matrix-LSTM is a time-surface reconstruction layer that can learn an effective integration process regardless on the objective loss to optimize. To showcase the flexibility of the proposed mechanism, we tested it on two different tasks: a high-level task, i.e., object classification (see Section A) and a low-level one, i.e., optical flow estimation (see Section 4.2) where the network is required to extract effective temporal features. We evaluated the goodness of the extracted representation indirectly: a state-of-the-art architecture is taken as a reference and the proposed method is evaluated in terms of the gain in performance obtained by replacing the network representation with a Matrix-LSTM.

4.1. Object classification

We evaluated the model on the classification task using two publicly available event-based collections, namely the N-Cars [40] and the N-Caltech101 [31] datasets. N-Cars is a collection of urban scenes recordings (lasting 100ms each) captured with a DVS sensor and showing two object categories: cars and urban background. The dataset comes already split into 7,940 car and 7,482 background training samples, and 4,396 car and 4,211 background testing samples. The N-Caltech101 collection is an event-based conversion of the popular Caltech-101 [22] dataset obtained by moving an event-based camera in front of a still monitor showing one of the original RGB images. Like the original version, the dataset contains objects from 101 classes distributed amongst 8,246 samples.

Network Architectures. We used two network configurations to test Matrix-LSTM on both datasets, namely the classifier used in Events-to-Video [34], and the one used to evaluate the EST [13] reconstruction. Both are based on ResNet [15] backbones and pre-trained on ImageNet [9]. Events-to-Video [34] uses a ResNet18 configuration maintaining the first 3 channels convolution (since reconstructed images are RGB) while adding an extra fully-connected layer to account for the different number of classes in both N-Caltech101 and N-Cars (we refer to this configuration as *ResNet-Ev2Vid*). EST [13] instead uses a ResNet34 backbone and replaces both the first and last layers respectively, with a convolution matching the input features, and a fully-connected layer with the proper number of neurons (we refer to this configuration as *ResNet-EST*).

To perform a fair comparison we replicated the two settings, using the same number of channels in the event representation (although we also tried different channel values) and data augmentation procedures (random horizontal flips and crops of 224×224 pixels). We perform early stopping on a validation set in all experiments, using 20% of the training on N-Cars and using the splits provided by the EST official code repository [12] for N-Caltech101. ADAM [18] was used as optimizer for all experiments with a learning rate of 10^{-4} . Finally, we use a batch size of 64 and a constant learning rate on N-Cars in both configurations. On N-Caltech101, instead, we use a batch size of 16 while decaying the learning rate by a factor of 0.8 after each epoch when testing on *ResNet-Ev2Vid*, and a batch size of 100 with no decay with the *ResNet-EST* setup. Finally, to perform a robust evaluation, we compute the mean and standard deviation values using five different seeds in all the experiments reported in this section.

4.1.1 Results

The empirical evaluation is organized as it follow for both *ResNet-Ev2Vid* and *ResNet-EST* configurations. We al-

Table 1. Results on N-Cars with [34] ResNet18–Ev2Vid, variable time encoding, and normalization.

| ResNet Norm | ts absolute | ts relative | delay relative |
|-------------|----------------------|---------------|----------------------|
| ✓ | 95.22 ± 0.41% | 94.77 ± 1.01% | 95.40 ± 0.59% |
| | 95.75 ± 0.27% | 95.32 ± 0.85% | 95.80 ± 0.53% |

Table 2. Results on N-Cars with [13] ResNet18–EST with variable time encoding and number of bins.

| | | 1 bin | 2 bins | 9 bins |
|-------|-----------------|---------------|----------------------|----------------------|
| delay | ts glob. + loc. | - | 92.68 ± 1.23% | 92.32 ± 1.02% |
| | local | 92.64 ± 1.21% | 92.35 ± 0.83% | 92.67 ± 0.90% |
| ts | ts glob. + loc. | - | 93.46 ± 0.84% | 93.21 ± 0.49% |
| | local | 92.65 ± 0.78% | 92.75 ± 1.38% | 93.12 ± 0.68% |

ways perform hyper-parameters search using a ResNet18 backbone on N-Cars, since it is faster to train and thus it allows us to explore a larger combination of parameters. We then select the best configuration to train the remaining architectures, namely, ResNet34 on N-Cars and both variants on N-Caltech101.

Matrix-LSTM + ResNet-Ev2Vid. We start out with the *ResNet–Ev2Vid* baseline (setting up the Matrix-LSTM to output 3 channels) by identifying the optimal time feature to provide as input to the LSTM, as reported in Table 1. We distinguish between *ts* and *delay* features and between *absolute* and *relative* scope. The first distinction refers to the type of time encoding, i.e., the timestamp of each event in the case of *ts* feature, or the delay between an event and the previous one in case of *delay*. Time features are always range-normalized between 0 and 1, with the scope distinction differentiating if the normalization takes place before splitting events into pixels (*absolute* feature) or after (*relative* feature). In the case of *ts*, *absolute* means that the first and last events in the sequence have time feature 0 and 1, respectively, regardless of their position, whereas *relative* means that the previous condition holds for each position (x, y) . Note that we only consider relative delays since it is only meaningful to compute them between events of the same pixel. Finally, we always add the polarity, obtaining a 2-value feature $f_i^{(x,y)}$. *delay relative* and *ts absolute* are those providing the best results, with *ts relative* having higher variance. We select *delay relative* as the best configuration. In Table 1 we also show how the network performance changes when the frame normalization used while training the ResNet backbone on ImageNet is applied to the Matrix-LSTM output. While performing normalization makes sense in a setting where training images are very similar to those used in pretraining, as in Events-to-Video [34], we found out that in our case, where no constraint is imposed on the reconstruction visual aspect, this does not improve the performance.

Matrix-LSTM + ResNet-EST. We continue the experiments on N-Cars by considering the *ResNet–EST* configuration as the baseline, where we explore the effects of using bins, i.e., intervals, on the quality of the Matrix-LSTM reconstruction. As performed on the previous set of experi-

Table 3. Results on N-Cars with [13] ResNet18–EST, *polarity + global ts + local ts* encoding, optional SELayer and variable number of bins

| SE | 2 bins | 4 bins | 9 bins | 16 bins |
|----|----------------------|---------------|----------------------|---------------|
| ✓ | 93.46 ± 0.84% | 92.68 ± 0.62% | 93.21 ± 0.49% | 92.01 ± 0.45% |
| | 93.71 ± 0.93% | 92.90 ± 0.62% | 93.30 ± 0.47% | 92.44 ± 0.43% |

Table 4. Results on N-Cars with [13] ResNet18–EST, *polarity + global ts + local ts* encoding, SELayer and variable number of channels.

| n bins | Channels | | | |
|--------|---------------|---------------|---------------|----------------------|
| | 4 | 7 | 8 | 16 |
| 1 | 93.88 ± 0.87% | - | 93.60 ± 0.30% | 94.37 ± 0.40% |
| 2 | 93.05 ± 0.92% | - | 93.97 ± 0.52% | 94.09 ± 0.29% |
| 9 | 92.42 ± 0.65% | 93.56 ± 0.46% | 93.49 ± 0.84% | - |

ments, we first identify the best time encoding. Since multiple intervals are involved, we distinguish between *global* and *local* temporal features. The first type is computed on the original sequence \mathcal{E} , before splitting events into intervals, whereas the latter locally, within the interval scope \mathcal{E}_{τ_b} . For local features we consider the best options we identified with the ResNet-Ev2Vid configuration, namely *delay relative* and *ts absolute*, while we only consider *ts* as global feature since a global delay would lose meaning after interval splitting. Results are reported in Table 2 where values for single bin are missing since there is no distinction between *global* and *local* scope. Adding a global feature consistently improves performance. This can indeed help the LSTM network in performing integration conditioned on a global timescale and thus enabling the extraction of temporal consistent features. We select the *global ts + local ts* configuration in next experiments, since this provides slightly better performance and reduced variance, and always add the polarity as an additional feature.

The next set of experiments was designed to select the optimal number of bins, searching for the best $B = 2, 4, 9, 16$ as done in EST, while using a fixed *polarity + global ts + local ts* configuration. In these experiments, we also make use of a squeeze-and-excitation layer (SELayer) [17], a self-attention operation specifically designed to correlate channels. Note that in our configuration, being the number of channels limited, we always use a reduction factor of 1. Please refer to the paper [17] for more details. As reported in Table 3, adding the layer consistently improves performance. We explain this by noticing that surfaces computed on successive intervals are naturally correlated and, thus, explicitly modeling this behavior within the network structure, helps the model in extracting richer features. Having found the bin setup performing the best (namely $B = 2, 4$), and since our Matrix-LSTM module can produce a variable number of output features, we perform the last set of experiments to select the Matrix-LSTM hidden size (a parameter that also controls the number of output channels). Results are reported in Table 4. Note that we only consider 4, 7, 8 channels with 9 bins to limit the total number of channels after frame concatenation.

Table 5. Comparison between Matrix-LSTM best configurations and state-of-the-art.

| Method | Classifier | Channels (bins) | N-Cars | N-Caltech101 |
|---------------------------|----------------------|-----------------|---------------------|---------------------|
| H-First [32] | spike-based | - | 56.1 | 0.54 |
| HOTS [20] | histogram similarity | - | 62.4 | 21.0 |
| Gabor-SNN [40] | SVM | - | 78.9 | 19.6 |
| HATS [40] | SVM | - | 90.2 | 64.2 |
| | ResNet34-EST [13] | - | 90.9 | 69.1 |
| | ResNet18-Ev2Vid [34] | - | 90.4 | 70.0 |
| Ev2Vid [34] | ResNet18-Ev2Vid | 3 | 91.0 | 86.6 |
| Matrix-LSTM (Ours) | ResNet18-Ev2Vid | 3 (1) | 95.80 ± 0.53 | 84.12 ± 0.84 |
| | ResNet34-Ev2Vid | 3 (1) | 95.65 ± 0.46 | 85.72 ± 0.37 |
| EST [13] | ResNet34-EST | 2 (9) | 92.5 | 81.7 |
| | ResNet34-EST | 2 (16) | 92.3 | 83.7 |
| Matrix-LSTM (Ours) | ResNet18-EST | 16 (1) | 94.37 ± 0.40 | 81.24 ± 1.31 |
| | ResNet34-EST | 16 (1) | 94.31 ± 0.43 | 78.98 ± 0.54 |
| | ResNet18-EST | 16 (2) | 94.09 ± 0.29 | 83.42 ± 0.80 |
| | ResNet34-EST | 16 (2) | 94.31 ± 0.44 | 80.45 ± 0.55 |
| | ResNet18-EST | 2 (16) | 92.58 ± 0.68 | 84.31 ± 0.59 |
| | ResNet34-EST | 2 (16) | 92.15 ± 0.73 | 83.50 ± 1.24 |

Discussion. Results of the top performing configurations for both *ResNet-Ev2Vid* and *ResNet-EST* variants on both N-Cars and N-Caltech101 are reported in Table 5. We use *relative delay* with *ResNet-Ev2Vid* and *global ts + local ts* with *ResNet-EST*. Through an extensive evaluation, we show that using Matrix-LSTM representation as input to the baseline networks and training them jointly improve performance by a good margin. Indeed, using the ResNet34-Ev2Vid setup, our solution sets a new state-of-the-art on N-Cars, even surpassing the Events-to-Video model that was trained to extract realistic reconstructions, and that could, therefore, take full advantage of the ResNet pre-training. The same does not happen on N-Caltech101, whose performance usually greatly depends on pre-training also on the original image-based version, and where Events-to-Video has therefore advantage. Despite this, our model only performs 0.9% worse than the baseline. On the ResNet-EST configuration, the model performs consistently better on N-Cars, while slightly worse on N-Caltech101 on most configurations. However, we remark that search for the best configuration was indeed performed on N-Cars, while a hyper-parameter search directly performed on N-Caltech101 would have probably lead to better results.

4.2. Optical flow prediction

For the evaluation of optical flow prediction we used the MVSEC [49] suite. Fusing event-data with lidar, IMU, motion capture and GPS sources, MVSEC is the first event-based dataset to provide a solid benchmark for event camera in real urban conditions. The dataset provides ground truth information for depth and vehicle pose and was later extended in [48] with optical flow information extracted from depth-maps. The dataset has been recorded on a range of different vehicles and features both indoor and outdoor scenarios and different lighting conditions.

Network Architecture. We used the EV-FlowNet [48] architecture as reference model. To perform a fair comparison between the Matrix-LSTM representation and the hand-

crafted features used in the original architecture, we built our model on top of the publicly available codebase [47]. The code contains few minor upgrades over the paper version, but in our experiments, we made sure to first replicate the original network configuration. This consists of removing the batch normalization layers, setting to 2 the output channels of the layer preceding the optical flow prediction layer and disabling random rotations during training. For more details refer to the supplementary materials.

The original network uses a 4-channels event-surface, collecting in pairs of separate channels based on the event polarity, the timestamp of the most recent event, and the number of events occurred in every spatial location. We replaced this input representation with the Matrix-LSTM reconstruction mechanism, setting the output channels to 4 as well. We trained the model on the *outdoor_day1* and *outdoor_day2* sequences for 300,000 iterations, as in the original paper. We used the ADAM optimizer with batch size 8, and an initial learning rate of 10^{-5} , exponentially decayed every 4 epochs by a factor of 0.8. Test was performed on a separate set of recordings, namely *indoor_flying1*, *indoor_flying2* and *indoor_flying3*, which are visually different from the training data. The network performance is measured in terms of average endpoint error (AEE), defined as the distance between the endpoints of the predicted and ground truth flow vectors. In addition, as originally proposed in the KITTI benchmark [29] and as done in [48], we report the percentage of outliers, namely points with endpoint error greater than 3 pixels and 5% of the magnitude ground truth vector. Finally, following the evaluation procedure used in [48], we only report the error computed in spatial locations where at least one event was generated.

Results. In the previous classification experiments, we observed that the type of temporal features and the number of bins play an important role in extracting effective representations. We expect time resolution to be a key factor of performance in optical flow, hence, we focus here on measuring how different interval choices impact on the flow prediction. We decided to always use the *polarity + global ts + local ts* configuration, which worked well on N-Cars while considering different bin setups. To perform a fair comparison with Ev-FlowNet, that uses a 4-channels event-surface, we fix the hidden state of our LSTM to 4, and use the same training hyper-parameters as well. We noticed that EV-FlowNet is quite unstable at higher learning rates, while Matrix-LSTM could benefit from larger rates, so we multiply its learning rate, i.e., the Matrix-LSTM gradients, by a factor of 10 during training. Results are reported in Table 6.

As performed on classification, we study the effect of adding a SELayer on the best performing configuration. Correlating the intervals slightly improves the AEE metric in all test sequences but increases the number of outliers. As expected, varying the number of bins has a great im-

Table 6. Optical flow estimation on MVSEC

| Method | | <i>indoor_flying1</i> | | <i>indoor_flying2</i> | | <i>indoor_flying3</i> | |
|------------------------|------------------|-----------------------|--------------|-----------------------|--------------|-----------------------|--------------|
| | | AEE | %Outlier | AEE | %Outlier | AEE | %Outlier |
| Two-Channel Image [27] | | 1.21 | 4.49 | 2.03 | 22.8 | 1.84 | 17.7 |
| EV-FlowNet [48] | | 1.03 | 2.20 | 1.72 | 15.1 | 1.53 | 11.9 |
| Voxel Grid [50] | | 0.96 | 1.47 | 1.65 | 14.6 | 1.45 | 11.4 |
| EST [13] | exp. kernel | 0.96 | 1.27 | 1.58 | 10.5 | 1.40 | 9.44 |
| | learnt kernel | 0.97 | 0.91 | 1.38 | 8.20 | 1.43 | 6.47 |
| Matrix-LSTM (Ours) | 1 bin | 1.017 | 2.071 | 1.642 | 13.88 | 1.432 | 10.44 |
| | 2 bins | 0.829 | 0.471 | 1.194 | 5.341 | 1.083 | 4.390 |
| | 4 bins | 0.969 | 1.781 | 1.505 | 11.63 | 1.507 | 12.97 |
| | 8 bins | 0.881 | 0.672 | 1.292 | 6.594 | 1.181 | 5.389 |
| | 2 bins + SELayer | 0.821 | 0.534 | 1.191 | 5.590 | 1.077 | 4.805 |

impact on performance. The AEE metric, indeed, greatly reduces by simply considering two intervals instead of one. Interestingly, we achieved the best performance by considering only 2 intervals, as adding more bins hurts performance. We believe this behavior resides on the nature of optical flow prediction, where the network is implicitly asked to compare two distinct temporal instants. This configuration consistently improves the baseline up to 30.76% on *indoor_flying2*, highlighting the capability of the Matrix-LSTM to adapt also to low-level tasks where both spatial and temporal resolution are key factors for performance.

4.3. Time performance analysis

We compared the time performance of Matrix-LSTM with other event representations following EST [13] and HATS [40] evaluation procedure. In Table 7 we report the time required to compute features on a sample averaged over the whole N-Cars training dataset. The average forward pass time of Matrix-LSTM has been computed on both ResNet-Ev2Vid and ResNet-EST configurations using a GeForce GTX 1080Ti GPU. Our surface achieves similar time performance than both HATS and EST, performing only ≈ 2 ms slower than EST on the same configuration (9 bins and 2 channels). However, while EST can exploit parallel batch computation of events within the same sample, since each event feature is processed independently, Matrix-LSTM relies on sequential computation to reconstruct the surface. The custom CUDA kernels we designed in Section 3.2, however, enables each pixel sequence to be processed in parallel, drastically reducing the time required to process the whole sequence. Please, refer to the additional materials for more details.

In Figure 4 we analyze the accuracy-vs-latency trade-off on the N-Cars dataset, as proposed in [40], using the ResNet18-Ev2Vid configuration. While the performance of the model, trained on 100ms sequences, significantly drops when very few milliseconds of events are considered, the proposed method still shows good generalization, achieving better performance than the baselines when more than 20ms of events are used. However, fixing the performance loss on small latencies is just a matter of augmentation: by randomly cropping sequences to variable lengths (from 5ms to 100ms), our method consistently improves the baselines, dynamically adapting to sequences of different lengths.

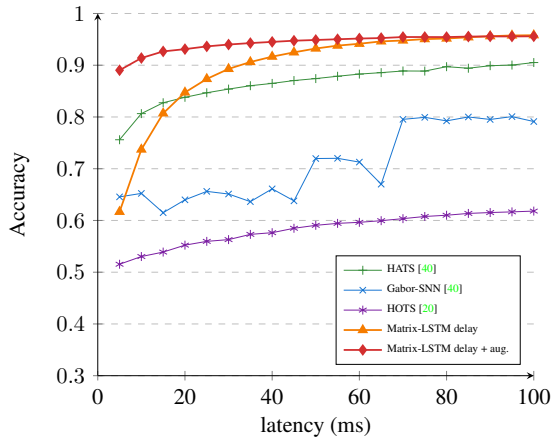


Figure 4. Accuracy as a function of latency (adapted from [40]).

Table 7. Average sample computation time on N-Cars and number of events processed per second.

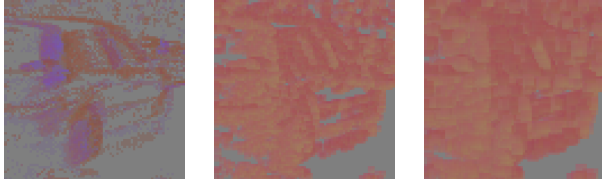
| Method | Bins | Channels | Asynch. | Time [ms] | Speed [kEV/s] |
|----------------|------|----------|---------|-------------|---------------|
| Gabor-SNN [40] | - | - | Yes | 285.95 | 14.15 |
| HOTS [20] | - | - | Yes | 157.57 | 25.68 |
| HATS [40] | - | - | Yes | 7.28 | 555.74 |
| EST [13] | 9 | 2 | No | 6.26 | 632.9 |
| Matrix-LSTM | 1 | 3 | No | 10.89 | 385.7 |
| (Ours) | 9 | 2 | No | 8.25 | 468.36 |

5. Conclusion

We proposed Matrix-LSTM, an effective method for learning dense event representations from event-based data. By modeling the reconstruction with a spatially shared LSTM we obtained a fully differentiable procedure that can be trained end-to-end to extract the event representation that best fits the task at hand. We proposed an efficient implementation of the method that exploits parallel batch-wise computation and demonstrates the effectiveness of the Matrix-LSTM layer on multiple tasks, improving the state-of-the-art of object classification on N-Cars by 3.3% and the performance on optical flow prediction on MVSEC by up to 23.07% over previous differentiable techniques [13]. Although we only integrate windows of events, the proposed mechanism can be extended to process a continuous streams thanks to the LSTM memory that is able to update its representation as soon as a new event arrives. As a future line of research, we plan to explore the use of Matrix-LSTM for more complex tasks such as gray-scale frame reconstruction [34], ego-motion and depth estimation [50, 45].

Table 8. Matrix-LSTM Resnet18-Ev2Vid performance on N-Cars with varying receptive field size and stride 1×1 .

| Receptive Field Size | | |
|----------------------|--------------------|--------------------|
| 1×1 | 3×3 | 5×5 |
| $95.80 \pm 0.53\%$ | $95.05 \pm 0.96\%$ | $94.38 \pm 0.64\%$ |



Acknowledgements We thank Alex Zihao Zhu for helping in reproducing EV-FlowNet original paper configuration. The research leading to these results has received funding from project TEINVEIN: TEcnologie INnovative per i VEicoli Intelligenti, CUP (Codice Unico Progetto - Unique Project Code): E96D17000110009 - Call “Accordi per la Ricerca e Innovazione”, cofunded by POR FESR 2014-2020 (Programma Operativo Regionale, Fondo Europeo di Sviluppo Regionale Regional Operational Programme, European Regional Development Fund).

Appendix A. Receptive Field Size

The operation performed by the Matrix-LSTM layer can be rephrased as a kernel convolution on the stream of events after being grouped by location. A recurrent filter, i.e., the shared LSTM unit, is applied on each 2D location (x, y) and a single value, aggregating all events occurred in (x, y) , is produced as output. As in a conventional convolution operation, the Matrix-LSTM can be convolved on the input space using different strides and receptive field dimensions.

In particular, given a receptive field of size $K_H \times K_W$, each LSTM cell processes a local neighborhood of asynchronous events $\mathcal{E}^{(x,y)} = \{(x_i, y_i, t_i, p_i) \mid t_i \in \tau, |x - x_i| < K_W - 1, |y - y_i| < K_H - 1\}$. Events features are computed as in the original formulation, however, an additional coordinate feature (p_x, p_y) is also added specifying the relative position of each event within the receptive field. Coordinate features are range-normalized in such a way that an event occurring in the top-left pixel of the receptive field has feature $(0, 0)$, whereas one occurring in the bottom-right position has features $(1, 1)$. Events belonging to multiple receptive fields (e.g., when the LSTM is convolved with a stride 1×1 and receptive field size greater than 1×1) are processed multiple times, independently.

In Table 8 we show how different choices of receptive field size impact classification accuracy on the N-Cars [40] datasets using the ResNet18-Ev2Vid configuration with *relative delay* encoding. Although in this extended formulation the LSTM cell has richer information to describe the local dynamics of the events within each spatial location, performance generally decreases by enlarging the receptive

field size. Event surfaces produced by the Matrix-LSTM layer are indeed more blurry and this may prevent the subsequent ResNet backbone from extracting effective features. Note that here we do not investigate different choices for the stride parameter since we want the Matrix-LSTM layer to only focus on extracting spatially rich event surfaces, without having to learn a downscale operation.

Appendix B. Time Performance

While the performance reported in Table 7 are computed on each sample independently to enable a fair comparison with the other methods, in Figure 5 and Figure 6 we study instead how the mean time required to process a sample over all the N-Cars training dataset and the corresponding events throughput change as a function of the batch size. Both performance dramatically increase when multiple samples are processed simultaneously in batch. This is crucial at training time, when optimization techniques greatly benefit from batch computation.

Furthermore, while increasing the number of output channels, for the same choice of batch size, increases the time required to process each sample (since the resulting Matrix-LSTM operates on a larger hidden state), increasing the number of bins has an opposite behaviour. Multiple intervals are indeed processed independently and in parallel by the Matrix-LSTM that has to process a smaller number of events in each spatial location, sequentially. In both configurations, finally, increasing the batch size reduces the mean processing time.

Appendix C. Optical Flow Prediction

C.1. Ev-FlowNet Baseline Results

We performed optical flow experiments starting from the publicly available Ev-FlowNet codebase [47] and replacing the original hand-crafted features with the proposed Matrix-LSTM layer. We first made sure to revert the baseline architecture to the original configuration, checking that we were able to replicate the paper results. Indeed, the public code contains minor upgrades over the paper version. We contacted the authors that provided us with the needed modifications. These consist of removing the batch normalization layers, setting to 2 the number of output channels of the layer preceding the optical flow prediction layer, and disabling random rotations during training. For completeness, we report the results we obtained by training the baseline from scratch with these fixes in Table 9.

To test how the network adapts to different flow magnitudes, the Ev-FlowNet [48] was tested on two evaluation settings for each test sequence: with input frames and corresponding events that are one frame apart (denoted as $dt=1$), and with frames and events four frames apart (denoted as $dt=4$). While we were able to closely replicate the results

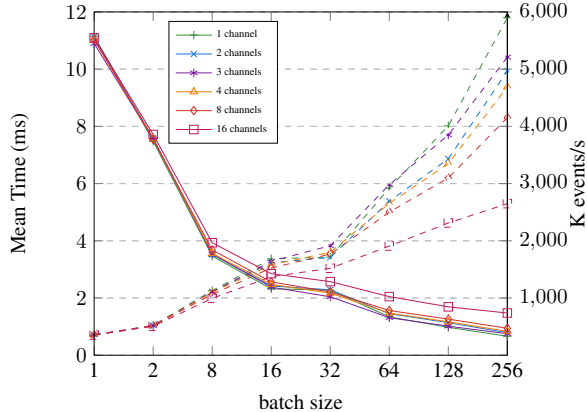


Figure 5. Number of processed events per second (dashed lines) and timing (solid lines) with varying number of channels.

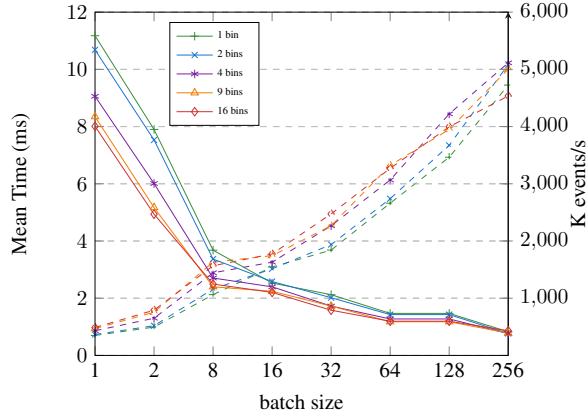


Figure 6. Number of processed events per second (dashed lines) and timing (solid lines) with varying number of bins.

Table 9. Effect of adding a Squeeze-and-Excitation layer on the optical flow prediction task.

| Method | | <i>indoor_flying1</i> | | | | <i>indoor_flying2</i> | | | | <i>indoor_flying3</i> | | | |
|-----------------------|------------------|-----------------------|--------------|--------------|---------------|-----------------------|--------------|--------------|---------------|-----------------------|--------------|--------------|---------------|
| | | <i>dt=1</i> | | <i>dt=4</i> | | <i>dt=1</i> | | <i>dt=4</i> | | <i>dt=1</i> | | <i>dt=4</i> | |
| | | AEE | %Outlier | AEE | %Outlier | AEE | %Outlier | AEE | %Outlier | AEE | %Outlier | AEE | %Outlier |
| Ev-FlowNet [48] | - | 1.03 | 2.2 | 2.25 | 24.7 | 2.12 | 15.1 | 4.05 | 45.3 | 1.53 | 11.9 | 3.45 | 39.7 |
| Ev-FlowNet (ours) | - | 1.015 | 2.736 | 3.432 | 48.685 | 1.606 | 12.089 | 5.957 | 63.226 | 1.548 | 11.937 | 5.247 | 57.662 |
| Matrix-LSTM (Ours) | 1 bin | 1.017 | 2.071 | 3.366 | 42.022 | 1.642 | 13.89 | 5.870 | 65.379 | 1.432 | 10.44 | 5.015 | 57.094 |
| | 2 bins | 0.829 | 0.471 | 2.269 | 23.558 | 1.194 | 5.341 | 3.946 | 42.450 | 1.083 | 4.390 | 3.172 | 31.975 |
| | 2 bins + SELayer | 0.821 | 0.534 | 2.378 | 25.995 | 1.191 | 5.590 | 4.333 | 45.396 | 1.077 | 4.805 | 3.549 | 36.822 |
| | 4 bins | 0.969 | 1.781 | 3.023 | 36.085 | 1.505 | 11.63 | 4.870 | 49.077 | 1.507 | 12.97 | 4.652 | 43.267 |
| | 4 bins + SELayer | 0.844 | 0.634 | 2.330 | 24.777 | 1.213 | 6.057 | 4.322 | 44.769 | 1.070 | 4.625 | 3.588 | 36.442 |
| | 8 bins | 0.881 | 0.672 | 2.290 | 24.203 | 1.292 | 6.594 | 3.978 | 42.230 | 1.181 | 5.389 | 3.346 | 33.951 |
| 8 bins + SELayer | 0.905 | 0.885 | 2.308 | 24.597 | 1.286 | 6.761 | 4.046 | 44.366 | 1.177 | 5.318 | 3.391 | 35.452 | |

of the first configuration ($dt=1$), with a minor improvement in the *indoor_flying2* sequence, the performance we obtain on the $dt=4$ setup is instead worse on all sequences, as reported on the first two rows of Table 9.

Despite this discrepancy, which prevents the Matrix-LSTM performance on $dt=4$ settings to be directly compared with the results reported on the Ev-FlowNet paper, we can still evaluate the benefits of our surface on larger flow magnitudes. Indeed, this work evaluates the Matrix-LSTM layer based on the relative performance improvement obtained by substituting the original features with our layer. Using our Ev-FlowNet results as baseline, we show that Matrix-LSTM is able to improve the optical flow quality even on the $dt=4$ setting, highlighting the capability of the layer to adapt to different sequence lengths and movement conditions. We report an improvement of up to 30.426% on $dt=1$ settings and up to 39.546% on $dt=4$ settings using our results as baseline.

C.2. Squeeze-and-Excitation Layer

Optical flow prediction is a complex task that requires neural networks to extract accurate features precisely describing motion inside the scene. An event aggregation mechanism is therefore required to extract rich temporal features from the events. In Section 4.2 of the paper we

show that time resolution is a key factor for extracting effective feature with Matrix-LSTM. In particular, increasing the number of bins has great impact on the predicted flow and allows the network to retain temporal information over long sequences. Here we focus, instead, on the effect of correlating temporal features by adding a SELayer to the Matrix-LSTM output. Table 9 reports the performance obtained using this additional layer on the MVSEC [49] task. The results we obtained show that adding an SELayer only improves performance on the 4 bins configuration for the $dt=4$ benchmark, while it consistently helps reducing the AEE metric on the $dt=1$ setting.

By comparing features obtained from subsequent intervals, the SELayer adaptively recalibrates features and helps modelling interdependencies between time instants, which is crucial for predicting optical flow. We believe that a similar approach can also be applied to other event aggregation mechanisms based on voxel-grids of temporal bins to improve their performance, especially those employing data driven optimization mechanisms [13].

Appendix D. Qualitative Results

The event aggregation process performed by the Matrix-LSTM layer is incremental. Events in each pixel location are processed sequentially; state and output of

the LSTM are updated each time. We propose to visualize the Matrix-LSTM surface as an RGB image by using the ResNet18-Ev2Vid configuration and interpreting the 3 output channels as RGB color. A video of such visualization showing the incremental frame reconstruction on N-Caltech101 samples is provided at this url: <https://drive.google.com/open?id=1KzhKKwJGXvMnhbg116gEArgYote7WW8V>. The same visualization technique is also used to display N-Cars Matrix-LSTM surfaces in Table 8.

We use a similar visualization technique to show optical flow predictions for *indoor_flying* sequences. Since we use our best performing model that uses 2 temporal bins, we decide to only show the first 3 channels of each temporal interval. Moreover, instead of visualizing how the event representation builds as new events arrive, we only show the frame obtained after having processed each window of events.

References

- [1] Martin Abadi, Paul Barham, Jianmin Chen, Zhifeng Chen, Andy Davis, Jeffrey Dean, Matthieu Devin, Sanjay Ghemawat, Geoffrey Irving, Michael Isard, Manjunath Kudlur, Josh Levenberg, Rajat Monga, Sherry Moore, Derek G. Murray, Benoit Steiner, Paul Tucker, Vijay Vasudevan, Pete Warden, Martin Wicke, Yuan Yu, and Xiaoqiang Zheng. Tensorflow: A system for large-scale machine learning. In *12th USENIX Symposium on Operating Systems Design and Implementation (OSDI 16)*, pages 265–283, 2016. 2
- [2] Raphael Berner, Christian Brandli, Minhao Yang, Shih-Chii Liu, and Tobi Delbruck. A 240×180 10mw 12us latency sparse-output vision sensor for mobile applications. In *2013 Symposium on VLSI Circuits*, pages C186–C187. IEEE, 2013. 1
- [3] Yin Bi, Aaron Chadha, Alhabib Abbas, Eirina Bourtsoulatz, and Yiannis Andreopoulos. Graph-based object classification for neuromorphic vision sensing. In *Proceedings of the IEEE International Conference on Computer Vision*, pages 491–501, 2019. 3
- [4] J. Botzheim, T. Obo, and N. Kubota. Human gesture recognition for robot partners by spiking neural network and classification learning. In *The 6th International Conference on Soft Computing and Intelligent Systems, and The 13th International Symposium on Advanced Intelligence Systems*, pages 1954–1958, Nov 2012. 2
- [5] Marco Cannici, Marco Ciccone, Andrea Romanoni, and Matteo Matteucci. Asynchronous convolutional networks for object detection in neuromorphic cameras. In *Proceedings of the IEEE Conference on Computer Vision and Pattern Recognition Workshops*, pages 0–0, 2019. 1, 2
- [6] Marco Cannici, Marco Ciccone, Andrea Romanoni, and Matteo Matteucci. Attention mechanisms for object recognition with event-based cameras. In *2019 IEEE Winter Conference on Applications of Computer Vision (WACV)*, pages 1127–1136. IEEE, 2019. 2, 3
- [7] Liang-Chieh Chen, George Papandreou, Iasonas Kokkinos, Kevin Murphy, and Alan L Yuille. Deeplab: Semantic image segmentation with deep convolutional nets, atrous convolution, and fully connected crfs. *IEEE transactions on pattern analysis and machine intelligence*, 40(4):834–848, 2017. 2
- [8] Gregory Kevin Cohen. *Event-Based Feature Detection, Recognition and Classification*. Theses, Université Pierre et Marie Curie - Paris VI, Sept. 2016. 1, 2
- [9] Jia Deng, Wei Dong, Richard Socher, Li-Jia Li, Kai Li, and Li Fei-Fei. Imagenet: A large-scale hierarchical image database. In *2009 IEEE conference on computer vision and pattern recognition*, pages 248–255. Ieee, 2009. 5
- [10] Peter U Diehl, Daniel Neil, Jonathan Binas, Matthew Cook, Shih-Chii Liu, and Michael Pfeiffer. Fast-classifying, high-accuracy spiking deep networks through weight and threshold balancing. In *2015 International Joint Conference on Neural Networks (IJCNN)*, pages 1–8. IEEE, 2015. 2
- [11] Guillermo Gallego, Tobi Delbruck, Garrick Orchard, Chiara Bartolozzi, Brian Taba, Andrea Censi, Stefan Leutenegger, Andrew Davison, Joerg Conradt, Kostas Daniilidis, et al. Event-based vision: A survey. *arXiv preprint arXiv:1904.08405*, 2019. 2
- [12] Daniel Gehrig, Antonio Loquercio, Konstantinos G. Derpanis, and Davide Scaramuzza. End-to-end learning of representations for asynchronous event-based data. https://github.com/uzh-rpg/rpg_event_representation_learning. 5
- [13] Daniel Gehrig, Antonio Loquercio, Konstantinos G. Derpanis, and Davide Scaramuzza. End-to-end learning of representations for asynchronous event-based data. In *IEEE International Conference of Computer Vision (ICCV)*, October 2019. 1, 2, 3, 4, 5, 6, 7, 8, 10
- [14] Kaiming He, Georgia Gkioxari, Piotr Dollár, and Ross Girshick. Mask r-cnn. In *Proceedings of the IEEE international conference on computer vision*, pages 2961–2969, 2017. 2
- [15] Kaiming He, Xiangyu Zhang, Shaoqing Ren, and Jian Sun. Deep residual learning for image recognition. In *Proceedings of the IEEE conference on computer vision and pattern recognition*, pages 770–778, 2016. 2, 5
- [16] Sepp Hochreiter and Jürgen Schmidhuber. Long short-term memory. *Neural computation*, 9(8):1735–1780, 1997. 1, 2, 3
- [17] Jie Hu, Li Shen, and Gang Sun. Squeeze-and-excitation networks. In *Proceedings of the IEEE conference on computer vision and pattern recognition*, pages 7132–7141, 2018. 4, 6
- [18] Diederik P. Kingma and Jimmy Ba. Adam: A method for stochastic optimization. *Int. Conf. on Learning Representations (ICLR)*, 2015. 5
- [19] Alex Krizhevsky, Ilya Sutskever, and Geoffrey E Hinton. Imagenet classification with deep convolutional neural networks. In *Advances in neural information processing systems*, pages 1097–1105, 2012. 2
- [20] Xavier Lagorce, Garrick Orchard, Francesco Galluppi, Bertram E Shi, and Ryad B Benosman. Hots: a hierarchy of event-based time-surfaces for pattern recognition. *IEEE transactions on pattern analysis and machine intelligence*, 39(7):1346–1359, 2016. 1, 2, 7, 8

- [21] Jun Haeng Lee, Tobi Delbruck, and Michael Pfeiffer. Training deep spiking neural networks using backpropagation. *Frontiers in Neuroscience*, 10:508, 2016. [2](#)
- [22] Li Fei-Fei, R. Fergus, and P. Perona. One-shot learning of object categories. *IEEE Transactions on Pattern Analysis and Machine Intelligence*, 28(4):594–611, April 2006. [5](#)
- [23] Patrick Lichtsteiner, Christoph Posch, and Tobi Delbruck. A 128×128 120 db $15\mu\text{s}$ latency asynchronous temporal contrast vision sensor. *IEEE journal of solid-state circuits*, 43(2):566–576, 2008. [1](#)
- [24] Wei Liu, Dragomir Anguelov, Dumitru Erhan, Christian Szegedy, Scott Reed, Cheng-Yang Fu, and Alexander C Berg. Ssd: Single shot multibox detector. In *European conference on computer vision*, pages 21–37. Springer, 2016. [2](#)
- [25] Jonathan Long, Evan Shelhamer, and Trevor Darrell. Fully convolutional networks for semantic segmentation. In *The IEEE Conference on Computer Vision and Pattern Recognition (CVPR)*, June 2015. [2](#), [4](#)
- [26] Wolfgang Maass. Networks of spiking neurons: the third generation of neural network models. *Neural networks*, 10(9):1659–1671, 1997. [2](#)
- [27] Ana I Maqueda, Antonio Loquercio, Guillermo Gallego, Narciso García, and Davide Scaramuzza. Event-based vision meets deep learning on steering prediction for self-driving cars. In *Proceedings of the IEEE Conference on Computer Vision and Pattern Recognition*, pages 5419–5427, 2018. [2](#), [8](#)
- [28] Boudjelal Meftah, Olivier Lezoray, and Abdelkader Benyettou. Segmentation and edge detection based on spiking neural network model. *Neural Processing Letters*, 32(2):131–146, 2010. [2](#)
- [29] Moritz Menze and Andreas Geiger. Object scene flow for autonomous vehicles. In *Conference on Computer Vision and Pattern Recognition (CVPR)*, 2015. [7](#)
- [30] Daniel Neil, Michael Pfeiffer, and Shih-Chii Liu. Phased lstm: Accelerating recurrent network training for long or event-based sequences. In *Advances in neural information processing systems*, pages 3882–3890, 2016. [1](#), [3](#)
- [31] Garrick Orchard, Ajinkya Jayawant, Gregory K Cohen, and Nitish Thakor. Converting static image datasets to spiking neuromorphic datasets using saccades. *Frontiers in neuroscience*, 9:437, 2015. [1](#), [2](#), [5](#)
- [32] Garrick Orchard, Cedric Meyer, Ralph Etienne-Cummings, Christoph Posch, Nitish Thakor, and Ryad Benosman. Hfirst: a temporal approach to object recognition. *IEEE transactions on pattern analysis and machine intelligence*, 37(10):2028–2040, 2015. [7](#)
- [33] Christoph Posch, Teresa Serrano-Gotarredona, Bernabe Linares-Barranco, and Tobi Delbruck. Retinomorph event-based vision sensors: bioinspired cameras with spiking output. *Proceedings of the IEEE*, 102(10):1470–1484, 2014. [1](#)
- [34] Henri Rebecq, René Ranftl, Vladlen Koltun, and Davide Scaramuzza. Events-to-video: Bringing modern computer vision to event cameras. In *Proceedings of the IEEE Conference on Computer Vision and Pattern Recognition*, pages 3857–3866, 2019. [1](#), [3](#), [4](#), [5](#), [6](#), [7](#), [8](#)
- [35] Joseph Redmon, Santosh Divvala, Ross Girshick, and Ali Farhadi. You only look once: Unified, real-time object detection. In *Proceedings of the IEEE conference on computer vision and pattern recognition*, pages 779–788, 2016. [2](#)
- [36] Bodo Rueckauer, Iulia-Alexandra Lungu, Yuhuang Hu, Michael Pfeiffer, and Shih-Chii Liu. Conversion of continuous-valued deep networks to efficient event-driven networks for image classification. *Frontiers in Neuroscience*, 11:682, 2017. [2](#)
- [37] Cedric Scheerlinck, Henri Rebecq, Timo Stoffregen, Nick Barnes, Robert Mahony, and Davide Scaramuzza. Ced: Color event camera dataset. In *Proceedings of the IEEE Conference on Computer Vision and Pattern Recognition Workshops*, pages 0–0, 2019. [3](#)
- [38] Yusuke Sekikawa, Kosuke Hara, and Hideo Saito. Eventnet: Asynchronous recursive event processing. In *Proceedings of the IEEE Conference on Computer Vision and Pattern Recognition*, pages 3887–3896, 2019. [3](#)
- [39] Teresa Serrano-Gotarredona and Bernabé Linares-Barranco. A 128×128 1.5% contrast sensitivity 0.9% fpn $3\mu\text{s}$ latency 4mw asynchronous frame-free dynamic vision sensor using transimpedance preamplifiers. *IEEE Journal of Solid-State Circuits*, 48(3):827–838, 2013. [1](#)
- [40] Amos Sironi, Manuele Brambilla, Nicolas Bourdis, Xavier Lagorce, and Ryad Benosman. Hats: Histograms of averaged time surfaces for robust event-based object classification. In *Proceedings of the IEEE Conference on Computer Vision and Pattern Recognition*, pages 1731–1740, 2018. [1](#), [2](#), [5](#), [7](#), [8](#), [9](#)
- [41] Benoit Steiner, Zachary DeVito, Soumith Chintala, Sam Gross, Adam Paszke, Francisco Massa, Adam Lerer, Gregory Chanan, Zeming Lin, Edward Yang, et al. Pytorch: An imperative style, high-performance deep learning library. *Advances in Neural Information Processing Systems*, 32, 2019. [2](#)
- [42] Christian Szegedy, Vincent Vanhoucke, Sergey Ioffe, Jon Shlens, and Zbigniew Wojna. Rethinking the inception architecture for computer vision. In *Proceedings of the IEEE conference on computer vision and pattern recognition*, pages 2818–2826, 2016. [2](#)
- [43] Qinyi Wang, Yexin Zhang, Junsong Yuan, and Yilong Lu. Space-time event clouds for gesture recognition: From rgb cameras to event cameras. In *2019 IEEE Winter Conference on Applications of Computer Vision (WACV)*, pages 1826–1835. IEEE, 2019. [3](#)
- [44] QingXiang Wu, Martin McGinnity, Liam Maguire, Ammar Belatreche, and Brendan Glackin. Edge detection based on spiking neural network model. In *International Conference on Intelligent Computing*, pages 26–34. Springer, 2007. [2](#)
- [45] Chengxi Ye, Anton Mitrokhin, Cornelia Fermüller, James A Yorke, and Yiannis Aloimonos. Unsupervised learning of dense optical flow, depth and egomotion from sparse event data. *arXiv preprint arXiv:1809.08625*, 2018. [3](#), [8](#)
- [46] Fisher Yu and Vladlen Koltun. Multi-scale context aggregation by dilated convolutions. *arXiv preprint arXiv:1511.07122*, 2015. [2](#)
- [47] Alex Zhu, Liangzhe Yuan, Kenneth Chaney, and Kostas Daniilidis. Ev-flownet: Self-supervised optical flow estima-

tion for event-based cameras. <https://github.com/daniilidis-group/EV-FlowNet>. 7, 9

- [48] Alex Zhu, Liangzhe Yuan, Kenneth Chaney, and Kostas Daniilidis. Ev-flownet: Self-supervised optical flow estimation for event-based cameras. In *Proceedings of Robotics: Science and Systems*, Pittsburgh, Pennsylvania, June 2018. 1, 2, 7, 8, 9, 10
- [49] Alex Zihao Zhu, Dinesh Thakur, Tolga Özaslan, Bernd Pfrommer, Vijay Kumar, and Kostas Daniilidis. The multivehicle stereo event camera dataset: An event camera dataset for 3d perception. *IEEE Robotics and Automation Letters*, 3(3):2032–2039, 2018. 2, 7, 10
- [50] Alex Zihao Zhu, Liangzhe Yuan, Kenneth Chaney, and Kostas Daniilidis. Unsupervised event-based learning of optical flow, depth, and egomotion. In *Proceedings of the IEEE Conference on Computer Vision and Pattern Recognition*, pages 989–997, 2019. 3, 4, 8